

PAPER

## Ring-like spatial distribution of laser accelerated protons in the ultra-high-contrast TNSA-regime

To cite this article: G A Becker *et al* 2018 *Plasma Phys. Control. Fusion* **60** 055010

View the [article online](#) for updates and enhancements.

### Related content

- [Robust energy enhancement of ultrashort pulse laser accelerated protons from reduced mass targets](#)  
K Zeil, J Metzkes, T Kluge *et al.*
- [Review of laser-driven ion sources and their applications](#)  
Hiroyuki Daido, Mamiko Nishiuchi and Alexander S Pirozhkov
- [Laser-driven ion acceleration via target normal sheath acceleration in the relativistic transparency regime](#)  
P L Poole, L Obst, G E Cochran *et al.*



**IOP | ebooks™**

Bringing you innovative digital publishing with leading voices to create your essential collection of books in STEM research.

Start exploring the collection - download the first chapter of every title for free.

# Ring-like spatial distribution of laser accelerated protons in the ultra-high-contrast TNSA-regime

G A Becker<sup>1</sup> , S Tietze<sup>2</sup>, S Keppler<sup>2</sup>, J Reislöhner<sup>1</sup>, J H Bin<sup>3,4</sup>, L Bock<sup>1</sup>, F-E Brack<sup>5</sup>, J Hein<sup>1</sup>, M Hellwing<sup>1</sup>, P Hitz<sup>3,4</sup>, M Hornung<sup>2</sup>, A Kessler<sup>2</sup>, S D Kraft<sup>5</sup> , S Kuschel<sup>2</sup>, H Liebetrau<sup>1</sup>, W Ma<sup>3,4</sup>, J Polz<sup>1</sup>, H-P Schlenvoigt<sup>5</sup> , F Schorcht<sup>2</sup>, M B Schwab<sup>1</sup>, A Seidel<sup>2</sup>, K Zeil<sup>5</sup>, U Schramm<sup>5,6</sup> , M Zepf<sup>2,7</sup>, J Schreiber<sup>3,4</sup>, S Rykovanov<sup>2</sup> and M C Kaluza<sup>1,2</sup>

<sup>1</sup> Institut für Optik und Quantenelektronik, Friedrich-Schiller-Universität Jena, Max-Wien-Platz 1, D-07743 Jena, Germany

<sup>2</sup> Helmholtz-Institut Jena, Fröbelstieg 3, D-07743 Jena, Germany

<sup>3</sup> Fakultät für Physik, Ludwig-Maximilians-Universität München, Am Coulombwall 1, D-85748 Garching, Germany

<sup>4</sup> Max-Planck-Institut für Quantenoptik, Hans-Kopfermann-Str. 1, D-85748 Garching, Germany

<sup>5</sup> Helmholtz-Zentrum Dresden-Rossendorf (HZDR), Bautzner Landstraße 400, D-01328 Dresden, Germany

<sup>6</sup> Technische Universität Dresden, D-01062 Dresden, Germany

<sup>7</sup> Centre for Plasma Physics, Queen's University Belfast BT7 1NN, United Kingdom

E-mail: [georg.becker@uni-jena.de](mailto:georg.becker@uni-jena.de)

Received 19 December 2017, revised 4 January 2018

Accepted for publication 1 March 2018

Published 3 April 2018



## Abstract

The spatial distribution of protons accelerated from submicron-thick plastic foil targets using multi-terawatt, frequency-doubled laser pulses with ultra-high temporal contrast has been investigated experimentally. A very stable, ring-like beam profile of the accelerated protons, oriented around the target's normal direction has been observed. The ring's opening angle has been found to decrease with increasing foil thicknesses. Two-dimensional particle-in-cell simulations reproduce our results indicating that the ring is formed during the expansion of the proton density distribution into the vacuum as described by the mechanism of target-normal sheath acceleration. Here—in addition to the longitudinal electric fields responsible for the forward acceleration of the protons—a lateral charge separation leads to transverse field components accelerating the protons in the lateral direction.

Supplementary material for this article is available [online](#)

Keywords: laser-plasma interaction, proton acceleration, proton beam profile, target normal sheath acceleration

(Some figures may appear in colour only in the online journal)

## 1. Introduction

The first experiments using high-intensity laser pulses to accelerate ions from thin foils to megaelectronvolt (MeV) energies [1, 2] have triggered a worldwide and ongoing interest in this field, leading to a large number of experimental

and theoretical investigations on laser-driven ion acceleration [3, 4]. This interest was also motivated by the prospect of potential future applications, such as hadron therapy [5] or as an ultra-short pulse frontend for conventional accelerators [6, 7], which would strongly benefit from the availability of compact—preferably table-top—ion accelerators. Most of

these applications, however, require an excellent control over the spectral and spatial characteristics of the generated proton beams, which laser-accelerated ion sources still lack. To improve the controllability and reproducibility, a deeper understanding of the physics underlying the ion-acceleration process is crucial.

The dominant process in most experiments on laser-driven ion acceleration, which have been performed so far, is target normal sheath acceleration (TNSA) [8]. In this scheme, a high-intensity laser ( $I_L \lambda_L^2 \geq 10^{18} \text{ W cm}^{-2} \mu\text{m}^2$ ) is focused onto a target, e.g. a few  $\mu\text{m}$  thick metal or plastic foil, ionizing the target front side and accelerating the freed electrons to kinetic energies in the multi-MeV range by the Lorentz force of the laser pulse. These electrons propagate through the foil and form an electron sheath at the target rear, leading to electric fields with  $\text{MV}/\mu\text{m}$  amplitudes between the sheath and the foil. This sheath field ionizes atoms at the target rear surface and accelerates the positive ions in the direction of the target normal. Protons are accelerated to the highest velocity due to their higher charge/mass ratio. So far, the highest proton energy achieved via TNSA is 85 MeV [9].

Beyond TNSA, there are other acceleration mechanisms under investigation, many of which require the use of sub-micron or few nm thick foils. One acceleration mechanism that was predicted to dominate for such ultra-thin targets irradiated by ultra-intense laser pulses is radiation pressure acceleration (RPA) [10, 11]. In this scenario, the light pressure of the laser pulse pushes electrons in the forward direction. As a consequence, they pull along the positive ions from the front surface. This process, also known as hole-boring, occurs irrespective of the target thickness. However, if the target is thin enough, the laser can drill a hole through the entire foil and for the rest of its duration directly transfer its momentum to the thin layer of electrons, which has been pushed out of the target. This opaque electron layer now acts as a light-sail [12, 13]. If the laser pulse is intense enough to accelerate the plasma electrons to relativistic energies, their effective mass is increased to  $\gamma_e m_e$ , where  $m_e$  is the electrons' rest mass and  $\gamma_e$  is their associated Lorentz factor. As a consequence, a few-nm thin foil, which was opaque to the laser pulse (since the foil's electron density  $n_e$  exceeds the laser's critical density  $n_c = \omega_L^2 \epsilon_0 m_e / e^2$ ) may become completely or partially transparent due to the effective mass increase of the plasma electrons [14]. This effect, called relativistically induced transparency (RIT), reduces the efficiency of RPA but can also lead to volumetric acceleration [15]. This transparency enhanced sheath acceleration regime can be reached using laser pulses with  $\sim 100 \text{ J}$  pulse energy and a pulse duration  $\lesssim 1 \text{ ps}$ , as it was shown recently in experiments at the TRIDENT [16, 17] and VULCAN laser facilities [18–21]. However, for these experimental parameters TNSA and RPA are also present.

In order to distinguish between the various acceleration processes during an experiment, it is helpful to identify key features of the proton beams and assign their origin to these different processes. Besides measurements of the time-integrated spectra, e.g. with a Thomson-parabola spectrometer (TP), additional measurements of the spatial distribution of

the accelerated protons, usually carried out with radiochromic films (RCFs) or nuclear track detectors such as CR39, are advisable to reach this objective. The spatial profile is also relevant for the further transport and focussing of the proton beams in order to realize subsequent applications.

An intriguing feature, which has often been observed during laser-driven ion acceleration experiments, is a ring-like structure (RLS) of the low-energetic protons' spatial distribution. In experiments performed with the VULCAN-laser at the turn of the millenium, a RLS was found during the interaction of a  $50 \text{ J}/1 \text{ ps}$  pulse with  $\sim 100 \mu\text{m}$  thick aluminum foils [2, 22, 23]. The origin of the RLS was attributed to magnetic fields generated inside the foil by electron currents. Protons accelerated at the target *front side* then experience a deflection while propagating through magnetic fields inside the foil. Similar proton features could be observed in experiments at the GEKKO MII-laser where  $5 \mu\text{m}$ ,  $25 \mu\text{m}$  and  $100 \mu\text{m}$  thick plastic foils were used [24]. There, however, the RLS was explained to be formed by toroidal magnetic fields generated by electron currents within the rear-surface hot electron sheath, which deflected the protons originating from the target *back side*. Besides these observations, an RLS could also be observed at experiments with  $400 \text{ mJ}/42 \text{ fs}$  pulses of the THOR-laser whereas the RLS was related to a 'bell-shaped' electron sheath [25]. In recent experiments, a RLS has also been measured in high-contrast experiments in which the interaction with ultra-thin foils was investigated. At the TRIDENT-laser, experiments with  $\sim 100 \text{ nm}$  thick diamond-like carbon foil targets showed an RLS, which was explained in the context of RIT [17]. At the VULCAN-laser, aluminum foils were used and the observed RLS was explained to be the result of the interaction between aluminum ions and protons during a process including RIT [21].

The numerous observations and differing explanations from various experimental regimes identify the RLS as a key feature in high-intensity ion acceleration experiments. For this reason we present in this paper the results from detailed experimental investigations and particle-in-cell (PIC) simulations in order to identify the source of RLSs during the interaction of high-contrast laser pulses with ultra-thin foils. In the following section we explain our experimental setup, which includes a scintillator screen in combination with two gated CCD (G-CCD) cameras for online detection of the spatial proton distribution. The results of the experimental RLS-measurements including the RLS-dependence on the target orientation and thickness as well as the protons' kinetic energy are presented in section 3. In section 4 we present PIC simulations reproducing our experiment results. Based on the results of our simulations and the experimental data described in section 5 the RLS is a result of lateral charge separation occurring during the plasma expansion. The lateral charge separation induces a lateral electric field  $E_y$  from which protons gain a lateral momentum  $p_y$ . Since this field increases in the longitudinal direction—like the forward accelerating field  $E_x$ —protons which have a higher longitudinal momentum  $p_x$  experience a higher  $p_y$ , too. This leads to a large amount of protons having an approximately constant ratio of  $p_y/p_x$  and

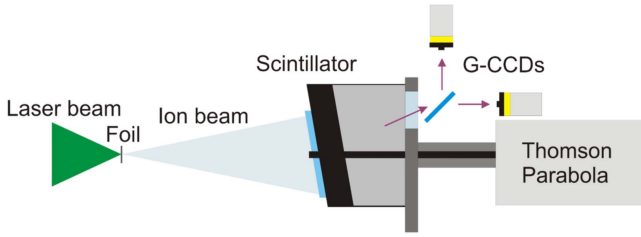


**Figure 1.** Schematic illustrating the ion diagnostic setup described in the text.

therefore to the focussing of many protons at a nearly constant angle  $\theta = \arctan(p_y/p_x)$  around the target normal direction.

## 2. Experimental setup

The experimental measurements were carried out at the POLARIS-laser, which is operated at the Friedrich-Schiller-University Jena and the Helmholtz-Institute Jena [26]. As targets, ultra-thin plastic foils with thicknesses ranging from 100 nm up to 800 nm were used. Since in experiments with nm-thick foils an extremely high temporal intensity contrast is required, the initial 1030 nm pulses were frequency-doubled by a 2 mm thick KDP-crystal. A detailed characterization of these laser pulses can be found in [27]. During the experimental campaign, POLARIS delivered frequency-doubled laser pulses at a central wavelength of  $\lambda_L \approx 515$  nm with an energy of  $E = (2.8 \pm 0.2)$  J and a full-width at half-maximum (FWHM)-duration of  $\tau = (135 \pm 25)$  fs. These pulses were linearly polarized in the vertical direction and focussed under normal incidence to a FWHM-spot-size of  $A = (8.8 \pm 0.9) \mu\text{m}^2$  containing  $(40 \pm 2)\%$  of the full pulse energy. This resulted in an average intensity of  $I_L = (9.4 \pm 2.2) \cdot 10^{19} \text{ W/cm}^2$  corresponding to an amplitude of the normalized vector potential  $a_0 = \sqrt{(I_L \lambda_L^2) / (1.37 \cdot 10^{18} \text{ Wcm}^{-2} \mu\text{m}^2)}$  between 3.8 and 4.7.

The experimental setup including the main proton diagnostics is shown in figure 1. To measure the spatial distribution of the accelerated protons, a fast responding plastic scintillator (BC-422Q by Saint Gobain) was utilized, which emits light after being hit by ionizing radiation. This scintillator has a signal rise time of 110 ps, a signal decay time of 700 ps and a signal pulse width of 360 ps (FWHM). The  $191 \times 191 \text{ mm}^2$  scintillator screen was positioned at a distance of 345 mm from the target and thus covered a full angle in the horizontal plane of  $31^\circ$ . The scintillator was protected against laser radiation with a  $15 \mu\text{m}$  thick aluminum foil. This aluminum foil was imaged onto a camera to observe if laser light was transmitted through the target foils. However, no transmitted light could be detected during the experiment which means the foils did not undergo RIT.

Note that the scintillator was tilted in the vertical direction by  $20^\circ$  to avoid back reflections of the laser light, which implies a slightly smaller vertical detection angle. In order to measure emitted light due to the accelerated protons only, the

scintillator rear surface was imaged onto two gateable CCD-cameras (G-CCD, 4 PICOS, Stanford Computer Optics), which provide a minimum gate-time of 1 ns. Due to the different time-of-flight of accelerated electrons, protons or x-rays, the G-CCDs enable the observation of the protons' spatial profile in a certain energy interval  $E_{\min} \leq E_p \leq E_{\max}$  while avoiding the detection of light emitted by the scintillator due to incoming x-rays and MeV electrons. Thus, the combination of the scintillator screen and the G-CCDs acts like a spatially resolving time-of-flight spectrometer. For the sake of clarity energy intervals will hereafter be written as  $E_{\min}/E_{\max}$ .

In order to observe the proton distribution within the energy intervals of 1.3/1.5 MeV respectively 4.4/6.0 MeV, the gate-time of a G-CCD was set to  $\Delta t = 2$  ns, while the absolute time delay was set to  $t = t_0 + 19.1$  ns for one shot respectively to  $t = t_0 + 9.2$  ns for a second shot.  $t = t_0$  denotes the time at which the scintillator shows a spatially homogeneous response due to the detection of accelerated electrons with a velocity of  $v_e \approx c_0$ . However, due to the increasing target-scintillator distance from the centre position to the horizontal edges of the scintillator, the energy interval slightly shifts to 1.4/1.6 MeV and 4.5/6.4 MeV for the chosen time delays. The  $15 \mu\text{m}$  thick aluminum foil used to protect the scintillator against laser light also stops protons with  $E_{\text{kin}} \leq 1$  MeV and carbon ions with  $E_{\text{kin}} \leq 17$  MeV and thus prevents these particles from affecting the measurement [28]. To simultaneously measure the spectrum of the accelerated protons in a certain direction, the scintillator provides a hole and a subsequent small black tube, which was aligned along the laser-forward direction and protects the G-CCDs from laser light. Protons and ions could propagate through this tube and were detected by a Thomson-parabola spectrometer equipped with a micro channel plate detector (MCP, see figure 1).

## 3. Experimental results

In our experiments, we could successfully reproduce the RLS within the regime of high-contrast pulses interacting with nm-thick foils. In figure 2, a typical proton beam profile for a 100 nm thick plastic foil is shown for the integrated full energy spectrum ranging from 1 MeV to  $E_{\max} \approx 6.2$  MeV. For a verification of the scintillator signal we measured one part of the proton beam's spatial distribution with the scintillator and the other part with a CR-39, which was placed in front of the scintillator. As depicted in figure 2, both measurements yield identical results which confirms that the scintillator is well-suited for the online detection of the spatial proton beam profile.

To determine whether the RLS is a result of plasma expansion within the TNSA-regime or a feature of RPA or RIT we investigated its orientation with respect to the target normal direction. For this purpose, we rotated a 480 nm-thick foil around the vertical axis going through the laser's focus position and thus separated the target normal from the laser forward direction as shown by the sketches in figure 3. The

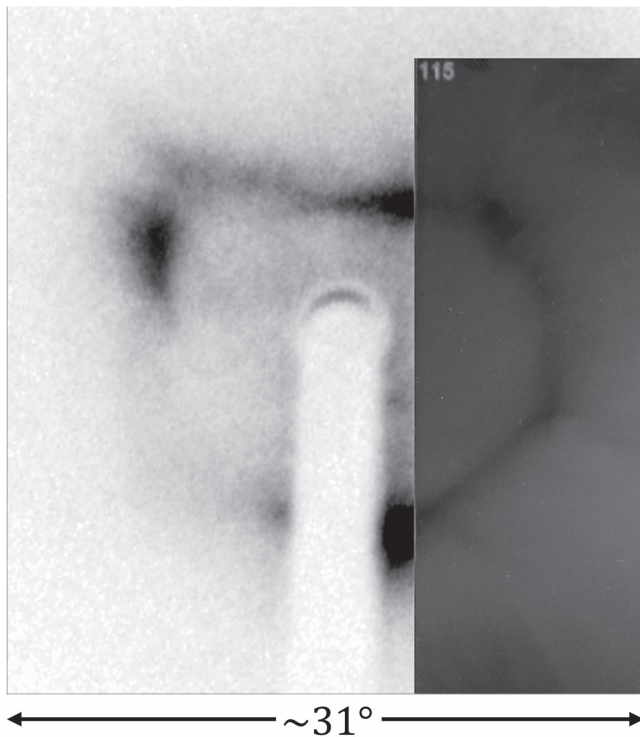


**Figure 2.** Spatial profile of the emitted protons for a 100 nm thick plastic foil showing the RLS. The left part was measured with the plastic scintillator and a G-CCD, while the right part was measured with a CR-39 placed in front of the scintillator. The scintillator and the CR39 were both shielded by a 15  $\mu\text{m}$  thick aluminum foil. The light ‘shadow’ in the centre of the scintillator is caused by the black tube, which protects the G-CCD cameras from laser light and plasma emission. Note that darker gray scales on both detectors correspond to a higher proton flux reaching a certain position on the detectors.

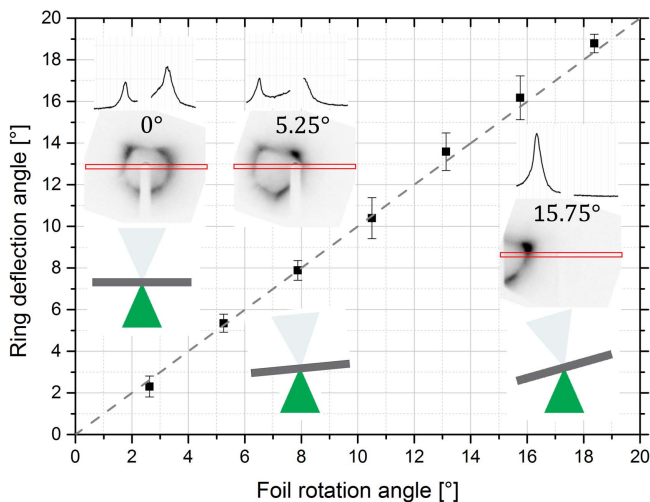


**Figure 3.** Deflection of the RLS depending on the rotation of a 480 nm CH foil. The RLS deflection angle was determined by considering the horizontal lineout taken within the red rectangle. The positions of the two RLS peaks within the lineout were analyzed relative to the non-rotated case. The black squares are averaged values over 2 to 4 shots (except for a single shot at 18.4°) for each rotation angle. Summing over all angles, 19 shots were taken in total. The error bars account for the standard deviation if more than one shot per angle was taken and the estimated systematic errors. The insets show the measured spatial proton profiles for a target rotation of 0°, 5.25°, and 15.75°.

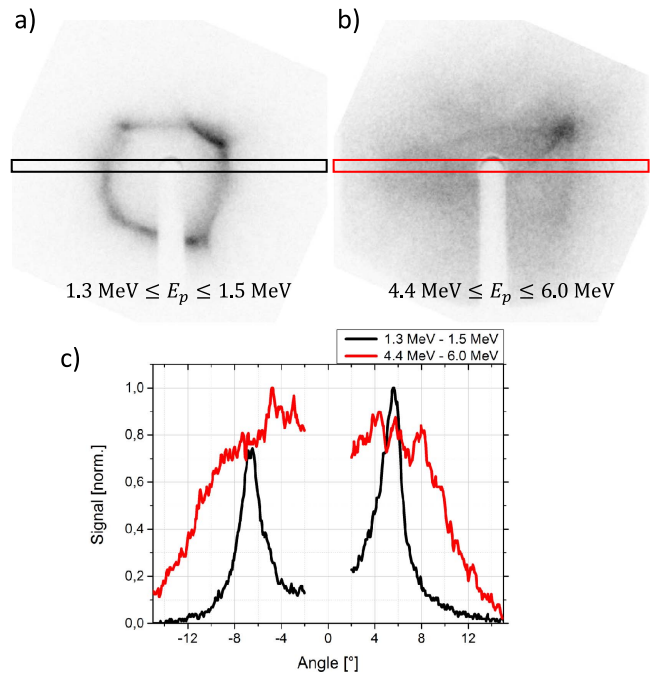


**Figure 4.** Measured proton beam profile for two different shots and two different energy intervals of (a) 1.3/1.5 MeV and (b) 4.4/6.0 MeV. (c) Normalized horizontal lineouts of the proton beam profiles taken within the rectangular boxes shown in (a) and (b). In these shots, maximum energies of  $E_{\text{max}} \approx 7.6$  MeV and  $\approx 8.3$  MeV were measured with the Thomson-parabola, respectively.

rotation angle was systematically increased from 0° to 18.4°. From the measurement of the RLS’s position, a one-to-one relation of the proton propagation direction and the foil rotation was obtained, which is depicted in figure 3. As a consequence, the protons forming the RLS are clearly accelerated in the target-normal direction and thus, can be assigned to proton acceleration within the TNSA-regime. Due to the fact that the RLS’s shape and signal strength are quite similar while separating the target normal from the laser forward direction, the underlying physics responsible for generating the RLS should be the same for the different angles, despite a possible change in electron heating mechanisms.

We also investigated the RLS-dependence on the proton energy by varying the measured energy interval by adjusting the absolute time delay of one of the G-CCD cameras. In order to ensure that the RLS was still present for the recorded shot, the second G-CCD was set to cover the full energy spectrum 1 MeV/ $E_{\text{max}}$ . Figures 4(a) and (b) show two measured profiles for energy intervals of 1.3/1.5 MeV and 4.4/6.0 MeV, respectively, while in both measurements comparable maximum proton energies of  $E_{\text{max}} \approx 7.6$  MeV and  $E_{\text{max}} \approx 8.3$  MeV were measured via the TP. From these two exemplary profiles it can be seen that the low-energy protons form a clear RLS, while for higher energies the ring structure smears out. For a better comparison, a normalized horizontal lineout for both profiles is shown in figure 4(c). The high-energy proton profile corresponds to a homogeneous distribution, which decreases to larger angles. The width of this distribution is slightly broader than the

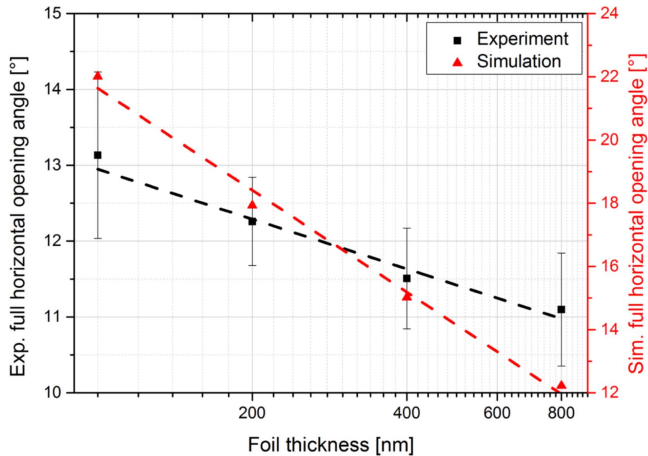


**Figure 5.** (Black) Measured opening angle  $\Theta$ , as the peak-to-peak angle difference of a horizontal lineout, as a function of the foil thickness. The error bars correspond to the standard deviation. The estimated systematic errors of the full horizontal opening angles are  $\approx 0.25^\circ$ . (Red) Opening angle  $\Theta$  obtained from the PIC-simulation for the energy interval  $1 \text{ MeV}/E_{\text{max}}$ .

peak-to-peak angle-difference of the RLS for low-energy protons. The peak-to-peak angle-difference  $\Theta = \theta_{\text{peak} > 0^\circ} - \theta_{\text{peak} < 0^\circ}$  is in the following referred to as the opening angle  $\Theta$ .

Finally, we investigated the behavior of the RLS depending on the target thickness. For this purpose we recorded the spatial distribution within the full detectable energy spectrum  $1 \text{ MeV}/E_{\text{max}}$ . Note that kinetic energies below  $1 \text{ MeV}$  could not be measured due to the aluminum shielding in front of the scintillator. In figure 5, the opening angle  $\Theta$  of the RLS versus the thickness of the used plastic foils ranging from  $100 \text{ nm}$  up to  $800 \text{ nm}$  is shown. With increasing target thickness,  $\Theta$  shows a continuous decrease. For the analysis,  $\Theta$  was determined from the individual lineouts, which were 11 for  $100 \text{ nm}$ , 4 for  $200 \text{ nm}$ , 6 for  $400 \text{ nm}$  and 6 for  $800 \text{ nm}$  and averaged afterwards.

#### 4. 2D PIC simulation

In order to obtain a comprehensive understanding of the generation of the RLS we have carried out 2D-particle-in-cell (2D-PIC) simulations using the fully relativistic EPOCH-code [29]. For these simulations, we used 50 particles per cell and a  $10\,000 \times 10\,000$  grid with a spatial extension in longitudinal direction of  $-5 \mu\text{m} \leq x \leq 45 \mu\text{m}$  and in the lateral direction of  $-25 \mu\text{m} \leq y \leq 25 \mu\text{m}$ . A Gaussian shaped laser pulse with  $d = 3 \mu\text{m}$  diameter focal spot (FWHM), a duration of  $\tau = 140 \text{ fs}$  (FWHM), and a central wavelength of  $\lambda_L = 515 \text{ nm}$  was used to approximate the experimental conditions. Furthermore, we considered linear polarization and a normalized vector potential of  $a_0 = 4.5$ . The peak of the laser pulse entered the simulation box at  $t_{\text{Peak}} = 322 \text{ fs}$ . In the simulations, we considered foils consisting of protons and fully ionized carbon ions with a ratio of 1:1. They had thicknesses of  $100 \text{ nm}$ ,  $200 \text{ nm}$ ,  $400 \text{ nm}$  and  $800 \text{ nm}$  with electron densities of  $90 \cdot n_c$ . The initial plasma

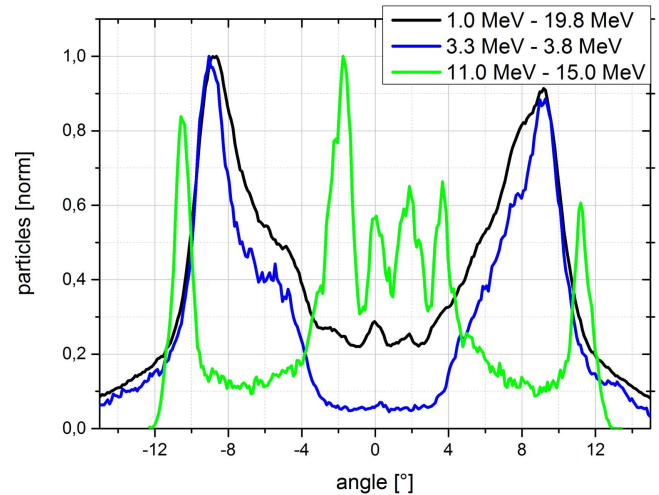


**Figure 6.** Normalized angular distributions of protons for three different energy intervals at  $t = t_{\text{Peak}} + 198 \text{ fs}$  extracted from a 2D-PIC simulation with a  $200 \text{ nm}$ -foil. The interval of  $1.0/19.8 \text{ MeV}$  (black line) corresponds to the full energy interval, which would be detectable with the plastic scintillator. Here,  $19.8 \text{ MeV}$  is the maximum proton energy  $E_{\text{max}}$  from the simulation for this foil thickness and time step.

temperature was set to  $k_B T = 1 \text{ keV}$ . The simulation was performed for an angle of incidence of  $0^\circ$  and the illuminated target surface was placed at  $x = 0$ . The total foil extent in the lateral direction was  $-20 \mu\text{m} \leq y \leq 20 \mu\text{m}$ .

For all foil thicknesses considered in the simulations, a two-peak structure in the angular distribution of the expanding protons could be observed, which would translate to an RLS in 3D geometry. In figure 6 we show the simulated protons' angular distribution for three different energy intervals for a  $200 \text{ nm}$  foil at  $t = t_{\text{Peak}} + 198 \text{ fs}$ . Here, the angular distribution for  $1 \text{ MeV}/E_{\text{max}}$  (black line) corresponds to the full energy spectrum, which would have been recorded experimentally to investigate the dependence of the opening angle  $\Theta$  on the foil thickness  $s$ . Within this interval we could reproduce the logarithmic thickness dependence as measured during the experiment (see figure 5, black data points) as shown in figure 5 (red). The difference in slope  $d\Theta/ds$  between the experimental and simulated values is most likely an effect of the 2D-simulation geometry. 2D simulations tend to overestimate the proton cut-off energies in contrast to 3D simulations [30]. This is probably due to the fact that the plasma can only expand in two rather than three dimensions which leads to higher particle densities and ultimately higher field strengths as compared to the experiment or 3D simulations. For this reason, the simulated maximum proton energies of  $\sim 19.8 \text{ MeV}$  are more than twice as high as those measured in the experiment ( $\sim 8.3 \text{ MeV}$ ).

To be able to compare the energy dependent spatial proton profile, the energy intervals considered in the experiment had to be adjusted to the higher simulated proton energies. For this reason, the boundaries of the energy intervals shown in figure 4 were higher by a factor of 2.5 for the simulation. The resulting angular distributions within the intervals  $3.3/3.8 \text{ MeV}$  and  $11.0/15.0 \text{ MeV}$  are shown in

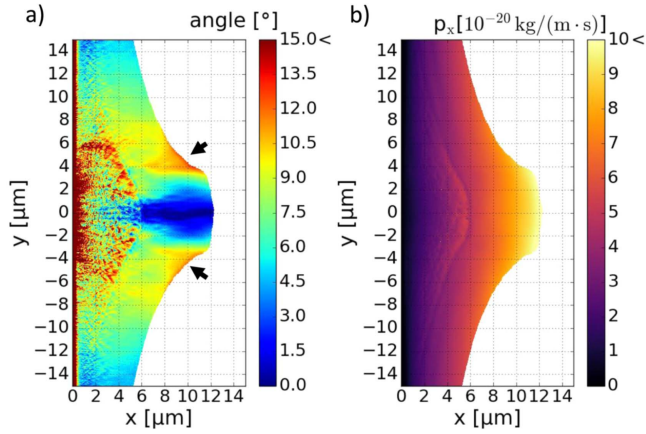


**Figure 7.** (a) 2D-spatial distribution of the proton deflection angle  $|\theta| = \arctan|p_y/p_x|$  for  $t = t_{\text{peak}} + 198$  fs. (b) The protons' longitudinal momentum ( $p_x$ ) for  $t = t_{\text{peak}} + 198$  fs.

figure 6 (blue and green). Compared to the measured profiles in figure 4, the simulated angular distributions in figure 6 agree well with the experimental data for both intervals except for the two sharp maxima at larger deflection angles of the high energy protons (figure 6 green). Here, the experiment shows a continuously decreasing signal towards larger angles, which is shown by the red line in figure 4(c). Hence, the 2D-PIC simulations could well reproduce the experimentally observed dependencies of the RLS regarding the proton energy and the target thickness.

## 5. Interpretation of the results

In figure 7, we show the 2D-spatial distribution of the proton deflection angle  $|\theta(x, y)| = \arctan|p_y/p_x|$  (a) and the associated longitudinal momentum  $p_x(x, y)$  (b) at  $t = t_{\text{peak}} + 198$  fs for a foil thickness of 200 nm. Here, the momentum  $p_x$  of the protons continuously increases in the positive  $x$ -direction. Protons having the highest momenta and kinetic energy  $E \approx p_x^2/(2m_p)$ , where  $m_p$  is the proton's mass, are located at the front of the proton distribution close to the target-normal axis  $y = 0$ . Here, the accelerating electric field component  $E_x$  has its maximum strength due to the highest density of hot electrons and thus the highest charge separation [8].

Figure 7(a) shows that protons near the target-normal ( $|y| < 2 \mu\text{m}$ ) axis have a small deflection angle, with this angle increasing when moving further away from the axis. However, protons at the outer regions ( $|y| > 10 \mu\text{m}$ ) again have a smaller deflection angle. As a consequence, protons forming the two-peak structure at  $\pm 9^\circ$  as shown in figure 6 for the same time step (black line) originate from  $2 \mu\text{m} \lesssim |y| \lesssim 10 \mu\text{m}$ . The angle also shows maxima at  $|y| \sim 5 \mu\text{m}$  and  $x \sim 9 \mu\text{m}$  (indicated by the arrows in figure 7(a)), which finally leads to the two-peak structure for protons within the energy interval 11.0/15.0 MeV at  $\pm 11^\circ$  in figure 6 (green line).

Figure 8(a) shows the temporal evolution of the lateral momentum  $p_y$ , while figure 8(b) shows the corresponding

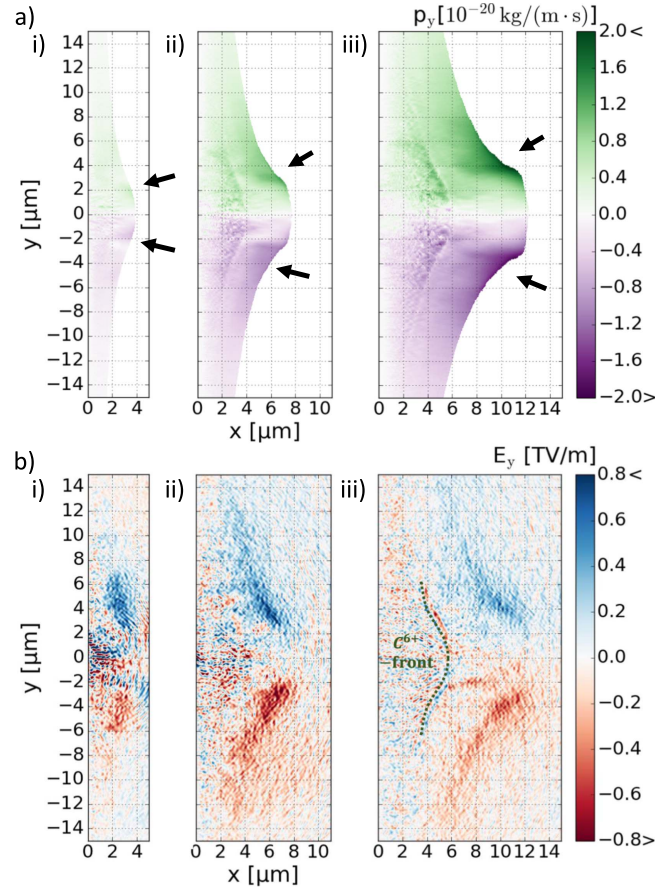


**Figure 8.** Temporal evolution of  $p_y$  (a) and  $E_y$  (b) for  $t = t_{\text{peak}} + 38$  fs (i),  $t = t_{\text{peak}} + 118$  fs (ii), and  $t = t_{\text{peak}} + 198$  fs (iii). Here, a 200 nm thick CH-foil was simulated.

transverse electric field component  $E_y$  at three different time steps (i–iii). The first time step at  $t = t_{\text{peak}} + 38$  fs (i) corresponds to the first time at which a two-peak structure can be clearly identified in the protons' angular distribution (not shown here). Within these three time steps (i–iii) a continuous increase of the absolute  $p_y$ -values in an increasing spatial region can clearly be observed. For each time step, these momenta continuously increase in the positive  $x$ -direction, where the highest momenta appear at the sides of the proton front, which are marked by the arrows in figure 8(a). The positions of these maximum values also correlate to the position of the highest deflection angle  $\theta_{\text{max}}$  in figure 7(a). Furthermore, figure 8(b) also shows a strong lateral electric field component in this region. The field strength increases during the time steps (i–iii) with a maximum at  $t = t_{\text{peak}} + 118$  fs (ii). For the last time-step (iii), the electric field component decreases again, but the protons have already gained the highest momentum. Both the lateral momentum and the lateral electric field show a zero crossing around the target-normal axis  $y \approx 0$  for all time steps, which ultimately leads to the emission of protons under small angles  $\theta \sim 0^\circ$  around the target normal.

For  $t = t_{\text{peak}} + 198$  fs, high frequency modulations can be seen close to the initial position of the foil's rear surface ( $x = 0.2 \mu\text{m}$ ) up to  $x \approx 6 \mu\text{m}$  within the intersection region of

protons and carbon. These modulations are present in the  $\theta$ - as well as in the  $p_x$ - and  $p_y$ -distribution and originate from density modulations of protons and carbon ions. The dip in the electric field ahead of the carbon front seen in figure 8(b)-(iii) modulates the proton spectrum as simulated by Robinson *et al* [31, 32] and observed in different experiments [33, 34]. To figure out, whether or not this expanding ion front influences the protons' angular distribution, an additional simulation was carried out with a 200 nm thick foil consisting of electrons and protons only. The angular distribution of the protons in this simulation again showed two significant peaks around  $\theta \approx \pm 11^\circ$  (see supplemental figures, available at [stacks.iop.org/PPCF/60/055010/mmedia](http://stacks.iop.org/PPCF/60/055010/mmedia)), which lets us conclude that the presence of a heavy ion species in the target is not the reason for the formation of the RLS.

From these results we can conclude that the lateral electric field component  $E_y$  at the position of the expanding proton front is responsible for the formation of the RLS during the interaction of a high-contrast laser pulse with a nm-thick foil. This can be understood as follows: at the beginning of the acceleration process, a charge separation field  $E_x$  is generated between the positively charged foil and the negatively charged electron sheath, which expands from the target rear side. The maximum field strength is reached close to the position opposite to the laser focus on the target front surface ( $y \approx 0$ ) and decreases in the lateral direction. In this field, protons from the target rear side are accelerated. As a result, the maximum proton energy can be observed around the axis ( $y \approx 0$ ) at the location of the maximum field strength and continuously decreases laterally. Therefore, protons near  $y \approx 0$  travel further into the vacuum than protons with  $|y| > 0$  during the same time interval. The profile of the curved expanding proton front also leads to a charge separation in lateral direction, which generates the electric field component  $E_y$ , as shown in figure 8(b). The strength and extension of this component strongly depend on the spatial width and local density of the proton distribution. In figure 8(a)–(i), the spatial width is small, which results in a highly localized region with a high field amplitude of the  $E_y$ -component and thus, a strong increase in the lateral momentum. During the subsequent expansion of the plasma, the spatial extent of the proton distribution continuously increases while the density decreases, which results in a decreasing field strength of  $E_y$ , as visible in figure 8(b)–(iii). Since both the lateral and longitudinal momentum  $p_y$  and  $p_x$  similarly increase from the foil's rear side to the front of the proton distribution, this leads to an emission of protons at a nearly constant angle  $\theta = \arctan(p_y/p_x)$ . Around the axis at  $y \approx 0$ , the lateral charge separation almost vanishes causing the protons to propagate at nearly  $0^\circ$ , in target-normal direction.

In figure 8(a), we plot the simulated field component  $E_y$  for the four different foil thicknesses used in the experiment at  $t = t_{\text{peak}} + 78$  fs. To compare the absolute field strength, the  $E_y$ -component was averaged for all simulated foil-thicknesses within the region indicated by the black rectangle in the lower left picture of figure 9(a). This averaged value is shown in

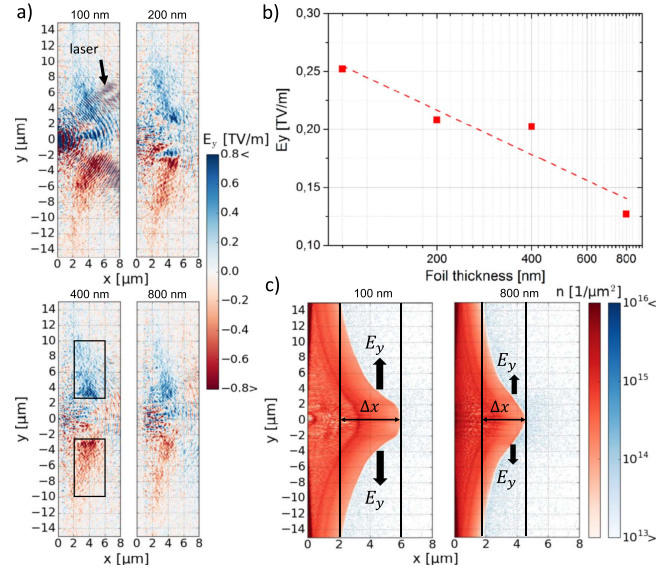


**Figure 9.** (a) Transverse component of the simulated electric field for the four foil thicknesses at  $t = t_{\text{peak}} + 78$  fs. (b) Shows the absolute value of the transverse field's amplitude averaged over the region marked by the black rectangle in (a). (c) Proton (red) and electron (blue) density distributions for 100 nm and 800 nm foils. Note that the initial positions of the foils' rear surface are located at  $x = 0 \mu\text{m}$  in (c).

figure 9(b). Here, we find that the averaged lateral field component  $E_y$  becomes weaker for increasing foil thickness, which can be explained as follows. The fast electrons, which set up the acceleration field  $E_x$  on the target's rear surface, first need to propagate from the front side through the target. Since the electron beam has a large divergence, the electron density on the rear side and thus the strength of the charge separation field  $E_x$  decreases with increasing target thickness. Consequently, this also leads to a reduced lateral charge separation field  $E_y$  during the proton expansion process. To illustrate this, the simulated electron- as well as the proton-density distributions are presented in figure 9(c) showing a 100 nm and a 800 nm foil at the same time step  $t = t_{\text{peak}} + 78$  fs. Looking at the on-axis protons ( $y = 0$ ) we find that for the 100 nm-foil, the protons experience a higher accelerating field and thus have traveled a longer distance  $\Delta x$  than off-axis protons at a time  $\Delta t$  as compared to the protons of the 800 nm-foil. Note, that in figure 9(c), the initial position  $x = 0$  is the target rear side. This leads to a different lateral charge separation and eventually to the decrease in the field strength (figure 9(b)). Consequently, a strong decrease of the lateral momentum  $p_y$ —stronger than the decrease of  $p_x$ —follows, ultimately leading to the decrease of the RLS-opening angle  $\Theta$  for increasing target thickness.

Potentially, this behavior might invert itself for foils of  $\lesssim 100$  nm as it was measured in [21] for aluminum foils. These experiments have shown the ring's diameter to decrease for thinner foils. Probably, this could be related to a reduction of the efficiency of the TNSA process for thinner foils or to a distortion of the charge separation field due to the breakthrough of the laser pulse. The latter can already be seen in the simulations with the 100 nm foil in figure 9(a) which

undergoes relativistic transparency during the interaction with the laser in contrast to the thicker foils. At this time-step, the field of the laser is already present (arrow), but has no significant effect on the appearance of the two peak structure in the simulation (see supplemental figures). It is likely, however, that for much thinner foils there will be a strong influence on size, form and appearance of the ring due to a more direct influence of the laser pulse on the electrons. A possible direct influence of the laser pulse to the RLS may already be present, since the RLS is somewhat shaped like a polygon (figures 2, 3 and 4). In an experiment with  $5\ \mu\text{m}$  to  $50\ \mu\text{m}$  thick gold foils [35], Schollmeier *et al* could detect a change in the proton beam profile as a consequence of a changing laser focus. They concluded that there is a direct imprint of the laser beam's intensity distribution on the electron beam forming the sheath at the target's rear surface. In our experiment the polygon shape of the RLS could therefore be due to a nonuniform intensity distribution of the laser near its focus. Although we assumed a Gaussian intensity distribution by measuring a calibrated equivalent focus [27], the real focus at full intensity could not be measured.

Our model fully explains our experimental observations. Since the accelerated protons initially expand normally to the target rear side, the lateral electric field component is always parallel to the foil's surface, eventually leading to the fixed relation of the orientation of the RLS and the target as shown in figure 3. Furthermore, the smearing of the RLS for higher proton energies, which is depicted in figure 4, directly results from the spatially localized range ( $y \approx 0$ ) of the highest field strengths of the accelerating field  $E_x$ . Within that range, the protons reach the highest kinetic energies, but hardly experience any lateral momentum since the strength of the lateral component of the electric field has a zero point in this region. Finally, the dependence of the RLS-opening angle on the thickness of the foil, which is shown in figure 5, can be explained by the thickness-dependent field strength of the  $E_y$  component.

## 6. Summary and outlook

In conclusion, we have shown that the RLS of the low-energy proton distribution is a key feature in the interaction of high-contrast laser pulses with nm-thick foils. The RLS arises due to lateral charge separation fields originating from the lateral profile of the proton expansion into vacuum. Our explanation very well describes the experimentally measured dependencies of the target orientation, the proton energy and the foil thickness and thus enables the clear determination of TNSA-accelerated protons also with the presence of further acceleration mechanisms like transparency enhanced sheath acceleration or RPA. Furthermore, the precise characterization of the RLS allows one to draw conclusions on the spatial profile of the proton density distribution during the acceleration process.

## Acknowledgments

The work leading to these results was partially supported by DFG (Grant No. TR18 B9 and No. KA 2869/2-1), by BMBF (Contracts No. 03Z1H531 and No. 05K16SJC) and by the European Union's Horizon 2020 Research and Innovation Programme (LASERLAB-EUROPE, grant no. 654148). Computational part of the paper was supported by the Helmholtz Association (Young Investigators Group VH-NG-1037). The authors gratefully acknowledge the following open-source projects: Numpy [36], Matplotlib [37], IPython [38], postpic [39].

## ORCID iDs

G A Becker  <https://orcid.org/0000-0002-9316-9125>  
 S D Kraft  <https://orcid.org/0000-0002-0638-6990>  
 H-P Schlenvoigt  <https://orcid.org/0000-0003-4400-1315>  
 U Schramm  <https://orcid.org/0000-0003-0390-7671>

## References

- [1] Snavely R A *et al* 2000 *Phys. Rev. Lett.* **85** 2945
- [2] Clark E, Krushelnick K, Zepf M, Beg F, Tatarakis M, Machacek A, Santala M, Watts I, Norreys P and Dangor A 2000 *Phys. Rev. Lett.* **85** 1654
- [3] Daido H, Nishiuchi M and Pirozhkov A S 2012 *Rep. Prog. Phys.* **75** 056401
- [4] Macchi A, Borghesi M and Passoni M 2013 *Rev. Mod. Phys.* **85** 751
- [5] Malka V, Faure J, Gauduel Y A, Lefebvre E, Rousse A and Phuoc K T 2008 *Nat. Phys.* **4** 447
- [6] Busold S *et al* 2015 *Sci. Rep.* **5** 12459
- [7] Dromey B *et al* 2016 *Nat. Commun.* **7** 10642
- [8] Wilks S, Langdon A, Cowan T, Roth M, Singh M, Hatchett S, Key M, Pennington D, MacKinnon A and Snavely R 2001 *Phys. Plasmas* **8** 542
- [9] Wagner F *et al* 2016 *Phys. Rev. Lett.* **116** 205002
- [10] Esirkepov T, Borghesi M, Bulanov S, Mourou G and Tajima T 2004 *Phys. Rev. Lett.* **92** 175003
- [11] Robinson A, Gibbon P, Zepf M, Kar S, Evans R and Bellei C 2009 *Plasma Phys. Control. Fusion* **51** 024004
- [12] Aurand B *et al* 2013 *New J. Phys.* **15** 033031
- [13] Kar S *et al* 2012 *Phys. Rev. Lett.* **109** 185006
- [14] Palaniyappan S *et al* 2012 *Nat. Phys.* **8** 763
- [15] Yin L, Albright B, Jung D, Shah R, Palaniyappan S, Bowers K, Henig A, Fernández J and Hegelich B M 2011 *Phys. Plasmas* **18** 063103
- [16] Jung D *et al* 2013 *New J. Phys.* **15** 023007
- [17] Jung D *et al* 2013 *New J. Phys.* **15** 123035
- [18] Powell H *et al* 2015 *New J. Phys.* **17** 103033
- [19] King M *et al* 2016 Nuclear Instruments and Methods in Physics Research section A: accelerators, Spectrometers Detectors and Associated Equipment **829** 163
- [20] Dover N *et al* 2016 *New J. Phys.* **18** 013038
- [21] Padda H *et al* 2016 *Phys. Plasmas* **23** 063116
- [22] Clark E L *et al* 2000 *Phys. Rev. Lett.* **84** 670
- [23] Zepf M *et al* 2003 *Phys. Rev. Lett.* **90** 064801
- [24] Murakami Y, Kitagawa Y, Sentoku Y, Mori M, Kodama R, Tanaka K A, Mima K and Yamanaka T 2001 *Phys. Plasmas* **8** 4138
- [25] Gaillard S, Fuchs J, Renard-Le Galloudec N and Cowan T 2007 *Rev. Sci. Instrum.* **78** 013304

- [26] Hornung M *et al* 2016 *Opt. Lett.* **41** 5413
- [27] Hornung M *et al* 2015 *Applied Sciences* **5** 1970
- [28] Ziegler J F, Ziegler M D and Biersack J P 2010 *Nuclear Instruments and Methods in Physics Research section B: Beam Interactions with Materials and Atoms* **268** 1818
- [29] Arber T *et al* 2015 *Plasma Phys. Control. Fusion* **57** 113001
- [30] Sgattoni A, Londrillo P, Macchi A and Passoni M 2012 *Phys. Rev. E* **85** 036405
- [31] Robinson A, Gibbon P, Pfotenhauer S, Jäckel O and Polz J 2009 *Plasma Phys. Control. Fusion* **51** 024001
- [32] Robinson A P L and Gibbon P 2007 *Phys. Rev. E* **75** 015401
- [33] Allen M *et al* 2003 *Phys. Plasmas* **10** 3283
- [34] Pfotenhauer S *et al* 2008 *New J. Phys.* **10** 033034
- [35] Schollmeier M *et al* 2008 *Phys. Plasmas* **15** 053101
- [36] Walt S V D, Colbert S C and Varoquaux G 2011 *Computing in Science & Engineering* **13** 22
- [37] Hunter J D 2007 *Computing In Science & Engineering* **9** 90
- [38] Pérez F and Granger B E 2007 *Computing in Science & Engineering* **9** 21–9
- [39] Kuschel S 2015 <http://github.com/skuschel/postpic>